Astronomy & Astrophysics manuscript no. ms_v8.2
February 26, 2014
©ESO 2014

LETTER TO THE EDITOR

Globular clusters of NGC 3115 in the near–infrared ⋆

Demonstrating the correctness of two opposing scenarios

Michele Cantiello[1], John P. Blakeslee[2], Gabriella Raimondo[1], Ana L. Chies-Santos[3], Zachary G. Jennings[4], Mark A. Norris[5], and Harald Kuntschner[6]

[1] INAF Osservatorio Astr. di Teramo, via Maggini, I-64100, Teramo, Italy e-mail: cantiello@oa-teramo.inaf.it
[2] Dominion Astrophysical Observatory, Herzberg Institute of Astrophysics, NRC of Canada, Victoria, Canada
[3] School of Physics and Astronomy, University of Nottingham, University Park, Nottingham NG7 2RD, UK
[4] University of California Observatories, Santa Cruz, CA 95064, USA
[5] Max Planck Institut fur Astronomie, Konigstuhl 17, D-69117, Heidelberg, Germany
[6] European Southern Observatory, Karl-Schwarzschild-Str. 2, D-85748 Garching bei München, Germany

Received —; accepted —

ABSTRACT

We combined new near-infrared VLT/HAWK-I data of the globular clusters (GCs) in the isolated edge-on S0 galaxy NGC 3115 with optical and spectroscopic ones taken from the literature, with the aim of analyzing the multiband GC color distributions. A recent study from the SLUGGS survey has shown that the GCs in this galaxy follow a bimodal distribution of Ca II triplet indices. Thus, NGC 3115 presents a critical example of a GC system with multiple, distinct, metallicity subpopulations, and this may argue against the "projection" scenario, which posits that the ubiquitous color bimodality mainly results from nonlinearities in the color-metallicity relations. Using optical, NIR, and spectroscopic data, we found strong and consistent evidence of index bimodality, which independently confirms the metallicity bimodality in NGC 3115 GCs. At the same time, we also found evidence for some color–color nonlinearity. Taken in the broader context of previous studies, the multicolor consistency of the GC bimodality in NGC 3115 suggests that in cases where GC systems exhibit clear differences between their optical and optical–NIR color distributions (as in some giant ellipticals), the apparent inconsistencies most likely result from nonlinearities in the color–metallicity relations.

Key words. galaxies: elliptical and lenticular, cD – galaxies: individual (NGC 3115)– galaxies: star clusters: general

arXiv:1402.6090v1 [astro-ph.GA] 25 Feb 2014

1. Introduction

The study of globular cluster (GC) systems in galaxies is one of the keystones for understanding the processes at the base of the formation and evolution of galaxies (Ashman & Zepf 1992; Brodie & Strader 2006). Recently, the interpretation of one of the most intriguing properties of GC systems in early-type galaxies, the nearly universal presence of two distinct peaks in the optical color distribution, has inspired a vigorous and prolific debate (Yoon et al. 2006; Kundu & Zepf 2007; Yoon et al. 2011; Chies-Santos et al. 2012; Blakeslee et al. 2012; Usher et al. 2012).

The importance of GC bimodality was recognized before it was a commonly observed property in early-type galaxies (ETGs, Schweizer 1987). Historically, the bimodal GC color in optical bands has been equated to metallicity ([Fe/H]) bimodality, implying a fundamental constraint on GC and galaxy formation scenarios. Metallicity bimodality requires two distinct epochs or mechanisms of formation, or both, for the blue (metal-poor) and red (metal-rich) GC subpopulations.

There are various proposed explanations for the GC color bimodality in ETGs: *dissipational* merging of spirals, in which a merger-formed population of red, metal-rich GCs is assumed to appear distinct from the blue, metal-poor GCs of the progenitor spirals (Ashman & Zepf 1992); the *dry* hierarchical assembly, which begins with a massive "seed" ETG that has a unimodal metal-rich GC distribution, and in which it is possible to produce a bimodal metallicity distribution through dissipationless accretion of many early-type dwarfs (Côté et al. 1998); and the *insitu* formation scenario (Forbes et al. 1997). Most of these proposed mechanisms, though, have assumed a simple linear conversion between [Fe/H] and color, which seemed justified from the small fractional age variations among the GCs (Cohen et al. 1998; Kuntschner et al. 2002; Puzia et al. 2005). However, this assumption became the subject of debate when three independent works, using observations and stellar population models, pointed out non-negligible nonlinearities in the color-metallicity relations of GCs (Peng et al. 2006; Richtler 2006; Yoon et al. 2006). In particular, Yoon and colleagues and Richtler demonstrated that these nonlinearities naturally produce bimodal color histograms from nonbimodal [Fe/H] distributions. This interpretation, dubbed the projection effect, provided an alternative explanation based on stellar evolution for the ubiquity of bimodal GC color distributions.

In this regard, Cantiello & Blakeslee (2007) suggested the use of multicolor GC histograms to verify the consistency of [Fe/H] distributions derived from different colors. These authors highlighted the role of optical to near-infrared (NIR) colors to distinguish between genuine bimodality in [Fe/H] and projected bimodality in color. If the nonlinear projection is at work, then the [Fe/H] distributions inferred from linear inversion of differ-

⋆ Based on observations made with ESO Telescopes at the La Silla Paranal Observatory under programme ID 60.A-9284. Tables 2-5 are only available in electronic form via http://www.edpsciences.org

ent color indices for the same GC sample will show some degree of inconsistency (discordant [Fe/H] peaks and/or fractions of GCs in each [Fe/H] component). The analysis of optical-to-NIR GC colors in various ETGs, as well as *u* to *z* photometry in some Virgo cluster members, indicates that the nonlinear projection effect is present at some level in these galaxies (Blakeslee et al. 2012; Chies-Santos et al. 2012; Yoon et al. 2011, 2013).

At the same time, the results of the SLUGGS survey[1], which collected spectra of $\sim$ 1000 GCs in 11 galaxies and derived [Fe/H] from the calcium II triplet index, CaT, support true [Fe/H] bimodality in at least some galaxies in addition to the Milky Way. Usher et al. (2012) found evidence for bimodal CaT distributions in six of eight galaxies with sufficient numbers of GC spectra. Nevertheless, the spectroscopically and photometrically derived [Fe/H] distributions show non-negligible differences in several galaxies of the SLUGGS sample, thus lacking the aforementioned multi-index coherence. However, the case of NGC 3115, an isolated lenticular galaxy at a distance of $\sim$ 10 Mpc (Tonry et al. 2001), revealed highly consistent [Fe/H] and color distributions, leading the authors to present this galaxy as a critical test of [Fe/H] bimodality (Brodie et al. 2012). Previous optical VLT FORS2 spectroscopy for 17 GCs in NGC 3115 showed hints of both a bimodal metallicity distribution *and* color or spectral index nonlinearity (Kuntschner et al. 2002), but it was limited by sample size.

In this Letter, we combine new NIR photometry with literature data to investigate the consistency of the bimodality in the optical, NIR, optical-NIR colors, and CaT, of the GCs in NGC 3115.

2. Observations

To analyze the properties of the GC system in NGC 3115, we took advantage of NIR observations with VLT/HAWK-I, HST/ACS optical photometry from Jennings et al. (2013) and spectroscopy from the SLUGGS survey (Usher et al. 2012).

All photometry is corrected for Galactic foreground-reddening using the Schlegel et al. (1998) maps, with recalibration from Schlafly & Finkbeiner (2011). To compare all data in the same photometric system, magnitudes were converted to AB mag using the zero points derived using the SYNPHOT task of IRAF/STSDAS and the spectrum of Vega from the Kurucz (1993) atlas of stellar atmosphere models.

2.1. VLT/HAWK-I near-infrared data

We used HAWK-I science verification data. The observations were carried out in very good seeing conditions, with FWHM $\lesssim 0''.5$ in all three bands. The science observations centered on NGC 3115 were interleaved with sky exposures of equal exposure time. The total on-source exposure times were 480s in *J*, 960s in *H*, and 1620s in *Ks*.

A series of custom IDL scripts was used to carry out the data reduction. Briefly, this consisted of subtracting dark exposures, producing super-sky flats from the stacked, unregistered sky exposures, and applying the derived flats to the individual science and sky exposures. Finally, individual exposures were registered and coadded.

Because it is difficult to model the disk component of the galaxy, we adopted the approach described in Jordán et al. (2004). After taking the logarithm of the galaxy image, we fitted two-dimensional bicubic splines to the brightness distribution using SExtractor (Bertin & Arnouts 1996). We then took the inverse logarithm of this model and subtracted it from the original image.

The photometry was then obtained from a second run of SExtractor on the residual image. Because of the very strong SBF signal (Tonry et al. 1990), we added the galaxy model times a filter-dependent constant to the SExtractor input *rms* map to avoid detecting surface brightness fluctuations as sources (see Jordán et al. 2004)[2]. To derive the absolute calibration, we compared our photometry catalogs with the 2MASS point source catalog. A total of 15 point sources in the *JH* frames, and 11 in *Ks* were used to derive the zero points, providing $zp_J = 25.75 \pm 0.06$ mag, $zp_H = 26.03 \pm 0.06$ mag, and $zp_{Ks} = 25.03 \pm 0.09$ mag. The list of matched sources is reported in Table 2.

2.2. Optical photometry and spectroscopy

We compared the NIR data with ACS optical photometry and with the SLUGGS data. The literature catalogs were selected on the basis of either the radial velocity or the spatial extent of the source or for both quantities. This allowed us to obtain GC catalogs with negligible contamination from fore- or background sources.

The SLUGGS survey is based on Subaru Suprime-Cam *gi* photometry and Keck/Deimos Ca II triplet measurements. The final sample of matched sources includes $N_{GC} = 88$ GCs (*HS* sample hereafter).

The ACS catalog consists of deep g_{F475W} and z_{F850LP} photometry. We paired our NIR catalog with the ACS one, which produced a sample of $N_{GC} = 264$ GC candidates (*HA* sample).

Finally, we also considered the sample of objects obtained by matching all three of the catalogs, which includes 74 GCs (*HSA* sample).

We analyzed the color and CaT distributions for the above three samples using the Gaussian mixture modeling code (GMM, Muratov & Gnedin 2010). This uses the likelihood-ratio test to compare the goodness of fit for double Gaussians versus a single Gaussian. For the best-fit double model, it estimates the means and widths of the two components, their separation DD in terms of combined widths, and the kurtosis *kurt* of the overall distribution. It also provides uncertainties based on bootstrap resampling.

3. Analysis of the color distributions

We analyzed the three samples mentioned in Section §2.2 by adopting the two different selection criteria described below. First, to coherently compare our results with the recent analysis by Brodie et al. (2012), we selected all GC candidates with CaT measurements with a signal-to-noise ratio > 12 Å^{-1} (sel#1 hereafter[3]). Second, for a consistent comparison of our analysis with a similar study of NGC 1399 GCs (Blakeslee et al. 2012), we selected only GCs within the magnitude range $20.5 \leq m_i\,(mag) \leq 22.5$, and photometric uncertainty on color $\Delta\,color \leq 0.07$ mag (sel#2).

[1] `http://sluggs.ucolick.org`.

[2] The constants were chosen to minimize the number of false detections. However, spurious objects are also removed when matching the NIR with optical photometric and spectroscopic catalogs (Section §2.2).

[3] Since the HA sample lacks the CaT measurements used to define the sample sel#1, in this case we chose to include only matching sources with $\Delta\,mag \leq 0.05$ in *all* HAWK-I and ACS passbands.

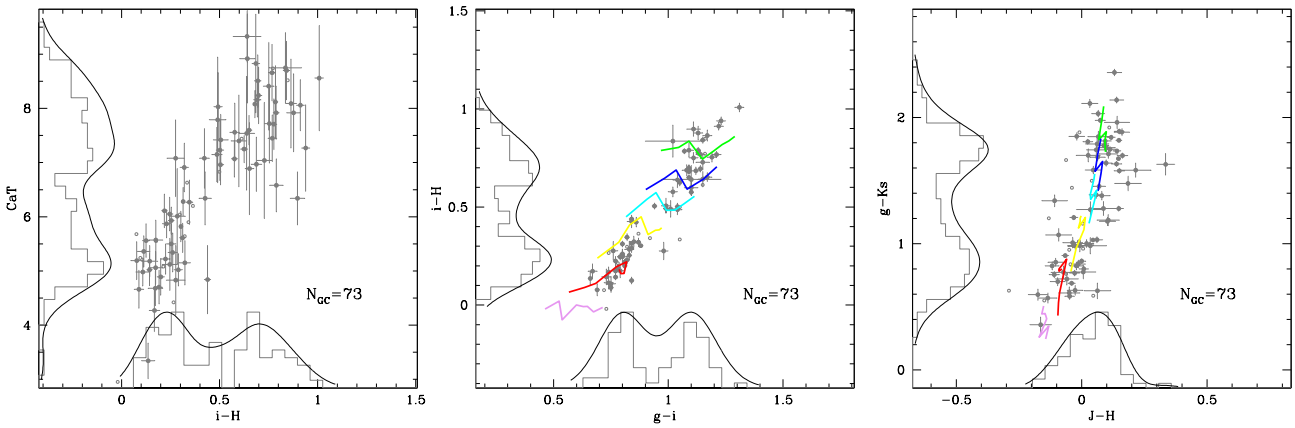

Fig. 1. Color-CaT and a selection of color-color diagrams for the HS sample (sel#1, full gray circles). Open circles mark GC candidates rejected by the adopted selection criteria. SPoT SSP models for [Fe/H]=−2.3 (pink), −1.3 (red), −0.7 (yellow), −0.3 (cyan), 0.0 (blue) and +0.3 (green) dex are also shown. The age range is $2 \leq t(Gyr) \leq 14$, at fixed metallicity younger ages have bluer color. Histograms, and nonparametric density estimates for histograms are also shown with arbitrary scale. (See electronic version of the Journal for a colour version of the figure.)

The results of the GMM tests on the three GC samples with the two different selection criteria are reported in Tables 3-4 and can be summarized as follows:

i) HS sample (sel#1) – The color-color and color-CaT diagrams for this sample and selection are shown in Figure 1. In general, the GMM results agree well for the various indices. However, for the purely NIR colors, the likelihood ratio test, $p(\chi^2)$, is consistent with a bimodal distribution in $J-Ks$ and $H-Ks$, while the p-values for the peak separation and kurtosis do not significantly favor bimodality.

ii) HA sample (sel#1) – Although the sample is nearly twice as large as the HS sample, the relevance of color bimodality in optical and optical-to-NIR data, and the lack of a strong evidence of bimodality in NIR colors is nearly identical to the previous case.

iii) HSA sample – The sample, contains 58 GC candidates in the case of sel#1 and returns GMM values consistent with the two previous samples (Figure 2).

iv) sel#1 versus sel#2– As expected, the results of GMM obtained using sel#1 or sel#2 are very similar for the HS and HSA samples. This is mostly a consequence of the small difference between the catalogs obtained when adopting one selection or the other. However, the similarity between selections #1 and #2 is also true for the HA sample, which is twice as large as sel#2, meaning that it reaches N_{GC} up to four times higher than some other samples or selections.

v) Although the values for the fraction of red GCs $f_{\rm red}$ derived from different samples, or selection, or colors are largely consistent, closer inspection shows the systematic nature of $f_{\rm red}$ with respect to galactocentric distance R_{GC}, that is, the radial gradient in mean GC color. In particular, for sel#1 we find $\langle f_{\rm red}^{HA} \rangle = 0.67 \pm 0.04$, while $\langle f_{\rm red}^{HS} \rangle = 0.55 \pm 0.04$[4]. Because the mean R_{GC} of the HA sample is smaller than that of the HS ($R_{GC}^{HA} \sim 16\%$ smaller), the difference in $f_{\rm red}$ for the two samples reflects the known tendency of red GCs to be more centrally concentrated than blue ones (Kissler-Patig 1997; Larsen & Brodie 2003).

A summary of the Tables 3-4 is reported in Table 1. The table gives the averaged p-values from the different samples, obtained from coupling all the optical colors (e.g. $g-i$; the column N_{col} gives the number of colors used for the average), all the optical-to-NIR (e.g. $g-H$), and all the NIR colors (e.g. $J-Ks$). The most profound result here, again, is the coherence between optical and optical-to-NIR colors, and the already mentioned lack of bimodality in NIR colors based on peak separation and kurtosis statistics.

Before moving on, we note that in some cases the GMM analysis indicates that three Gaussians are preferred to (or as good as) the double Gaussians model. The results of GMM fits with three components are reported in Table 5. Only cases where the least populated peak contains at least $\sim 10\%$ of the total population are considered. Although some colors for some samples are well fit with three Gaussians, we stress the lack of coherence in these tri-modal models for different colors.

4. Comparison with population models

Figures 1-2 show the integrated colors for simple stellar population (SSP) models from the SPoT group (Raimondo 2009)[5]. The model grid ranges from 2 to 14 Gyr in SSP age, and from −2.3 to +0.3 dex in [Fe/H]. Interpretation of integrated colors is hindered by the age-metallicity degeneracy (Worthey 1994). In this case, though, the broad wavelength coverage of the data and the higher sensitivity to [Fe/H] of optical-to-NIR colors compared with purely optical colors allows one to set more robust constraints on the stellar populations from the full set of color-color diagrams. Overall, the SSP models and the data agree well in general, and it is evident that the GC system covers almost the full metallicity range of the models.

In Figure 2 we show a color-color diagram for the HSA sample (sel#1). The sample from matching the three catalogs is smaller than the others considered above. However, the features observed in other samples are preserved, with lower scatter. Among these we highlight first, the absence of a GC component with $t \leq 8$ Gyr and [Fe/H] ≤ -2.3 dex, or even the complete lack of clusters with this or a lower metallicity. Second, on the high-metallicity regime, some GC candidates ($g_{F475W}-z_{F850LP} \geq 1.5$ and $i-H \geq 0.9$ mag) are consistent with [Fe/H]$\geq +0.3$ dex. The fraction of high-metallicity GC candidates is $\sim 5-10\%$. Other color-color diagrams also show a similar fraction of GCs above the [Fe/H]=0.3 dex limit[6].

[4] For the selection #2 we find $\langle f_{\rm red}^{HA} \rangle = 0.56 \pm 0.09$, and $\langle f_{\rm red}^{HS} \rangle = 0.52 \pm 0.06$.

[5] `http://www.oa-teramo.inaf.it/spot`

[6] Larger fractions, up to $\sim 15\%$, are implied by the $z-J$ or $z-H$ colors. The data-to-model mismatch might in part result from the uncertainty

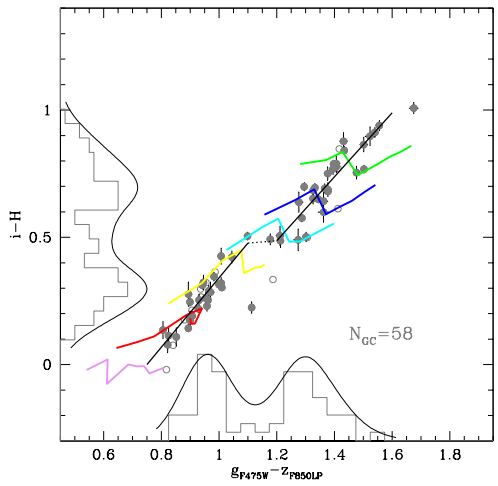

Fig. 2. Similar to Figure 1, but for the HSA sample. The solid black lines show linear least-squares fits to the GCs with $g_{F475W}-z_{F850LP} < 1.1$ and $1.2 < g_{F475W}-z_{F850LP} < 1.6$, respectively; the dotted nearly horizontal black line connects the endpoints of these fits. (See electronic version of the Journal for a colour version of the figure.)

Furthermore, while the bluer GCs appear to match the locus of SSP models for ages $t > 10$ Gyr, the red clusters are more consistent with $t < 10$ Gyr. However, the age sensitivity of the models is weak, and uncertainties in evolutionary *and* atmosphere models of AGB stars – such as low temperature opacity, the prescriptions for mass loss and dust – as well as the presence of extreme horizontal branch stars, might lead to artificial age differences. Nonetheless, the suggested trend agrees with other studies that found the metal-poor GCs to be 1–2 Gyr older than metal-rich ones (Puzia et al. 2005; Woodley et al. 2010).

An additional interesting feature of Figure 2 is the nonlinear shape of the color-color relation: at blue colors, $i-H$ increases steeply with $g_{F475W}-z_{F850LP}$; the dependence flattens at intermediate colors before becoming steep again. This is similar to the behavior found by Blakeslee et al. (2012) and resembles the quasi-inflection point present in color-metallicity relations, possibly indicating the shift in HB morphology around $i-H \sim 0.5$ mag (Yoon et al. 2006; Cantiello & Blakeslee 2007).

Finally, with regard to the dip in the color distributions, there is general agreement among the various color indices for a deficit of GCs in the $-1.2 \lesssim [Fe/H] \lesssim -0.4$ dex range. This confirms the results from the CaT index (Brodie et al. 2012) and indicates that CaT provides metallicity estimates consistent with integrated colors (when interpreted with the above models), at least at this intermediate [Fe/H] regime.

5. Discussion and conclusions

Our analysis of the GC system in NGC 3115 provides additional definitive proof of GC [Fe/H] bimodality in this S0 galaxy, the first to be firmly established beyond the Milky Way. Various studies have noted that to rule out the possibility that nonlinearities project a nonbimodal [Fe/H] distribution into a bimodal color distribution, one must recover consistent [Fe/H] distributions from multiple different photometric indices. In particular, Cantiello & Blakeslee (2007) showed that optical-to-NIR colors are the most useful in constraining the underlying metallicities. This is in part because the broad color baselines imply a lower sensitivity to the detailed shape of the index-metallicity relation; for the converse reason, bimodal [Fe/H] distributions may not be evident in the purely NIR colors. The present study confirms these expectations: *i*) the optical and optical-to-NIR colors are clearly bimodal and consistent with each other in terms of proportions of red and blue GCs, and *ii*) the pure NIR distributions give ambiguous results, in the sense that different colors and/or statistical indicators indicate the presence or lack of bimodality.

The comparison of GC colors with SSP models confirms earlier results (Brodie et al. 2012), using CaT as a proxy for metallicity, which derived a bimodal [Fe/H] distribution with a dip at $-1.3 \lesssim [Fe/H] \lesssim -0.3$ dex. The model comparison also suggests that the metal-rich GCs have slightly younger ages than the blue/metal-poor ones. Although this conclusion is subject to model uncertainties, the size of the age difference is consistent with that found between the metal-rich and metal-poor GCs in the Milky Way (VandenBerg et al. 2013).

Some previous studies of optical-to-NIR GC colors in giant ellipticals have found significantly different optical versus optical-to-NIR color distributions. For instance, using HST ACS and WFC3/IR data, Blakeslee et al. (2012) showed that while the optical color distributions of the Fornax giant elliptical NGC 1399 are clearly bimodal (supporting earlier results from Forte et al. 2005), the $V-H$ and $I-H$ distributions are not, or they imply significantly *different* bimodal breakdowns than found for the optical alone. Similarly, Chies-Santos et al. (2012) studied the *gzK* color distributions of 14 elliptical galaxies, mainly in the Virgo cluster, and reported that double-peaked color distributions are more common in $g-z$ than in the optical-NIR colors. Both studies found significant nonlinearity between the purely optical and optical-to-NIR colors, and both concluded that bimodal optical color distributions are not necessarily indicative of underlying bimodality in metallicity.

The lack of consistency between the purely optical and optical–NIR colors for NGC 1399 and some Virgo ellipticals contrasts strongly with the coherent color bimodality observed in NGC 3115, for which the metallicities are also clearly bimodal. In light of this contrast, and with the evidence for nonlinear color–color relations, the inconsistent optical and optical-NIR color bimodalities in some galaxies imply that nonlinearities do indeed play an important role in shaping the GC color distributions in those galaxies. Thus, while our multicolor photometric analysis confirms the [Fe/H] bimodality of NGC 3115 GCs, we conclude that the nonlinear projection effect remains a viable explanation for the *ubiquity* of optical color bimodality and is the

Table 1. Average results of GMM tests

Col. range	$p(\chi^2)(\pm)$	$p(DD)(\pm)$	$p(kurt)(\pm)$	$f_{\rm red}$ $(\pm)$	N_{cols}
GC selection #1					
Optical	0.00(0.02)	0.03(0.04)	0.00(<0.01)	0.55(0.02)	5
Opt.+NIR	0.00(0.04)	0.15(0.04)	0.00(0.01)	0.56(0.02)	24
NIR	0.20(0.09)	0.67(0.11)	0.92(0.06)	0.44(0.12)	9
GC selection #2					
Optical	0.00(0.01)	0.02(0.05)	0.00(<0.01)	0.56(0.02)	5
Opt.+NIR	0.00(0.03)	0.17(0.03)	0.00(0.01)	0.52(0.02)	24
NIR	0.07(0.11)	0.82(0.04)	0.94(0.07)	0.36(0.08)	9

in high-[Fe/H] SSP models for these colors that is caused by the partial overlap or proximity of the passbands and uncertainties in stellar atmosphere models in this wavelength regime. However, a similar fraction of GCs with [Fe/H] $\gtrsim 0.3$ dex was also found by Brodie et al. (2012) – we transformed their [Z/H] in [Fe/H] assuming the results of Tantalo et al. (1998), with $[\alpha/Fe] = 0.35$ (Pietrinferni et al. 2006). Moreover, these higher metal-rich fractions are for the HA sample, which is the most centrally concentrated of the considered samples (item (*iv*), section 3), and would therefore have the highest proportion of metal-rich GCs.

most likely cause in cases where the optical-NIR colors lack obvious bimodality.

In summary: *i*) optical and optical-to-NIR colors and CaT indices of GCs in NGC 3115 are bimodal; *ii*) the bimodal distributions derived for different photometric and spectroscopic indices show good consistency; *iii*) evidence for bimodality is weak or absent for purely NIR colors; *iv*) our results agree with model predictions for GC systems with truly bimodal [Fe/H] distributions, which provides definitive proof of [Fe/H] bimodality in NGC 3115, perhaps the first galaxy beyond the Local Group for which this is the case; *v*) comparison with SSP models confirms earlier metallicity results based on CaT indices; *vi*) despite the consistency of the color distributions, we also observe color-color nonlinearities, most clearly in the case of $i-H$ versus $g-z$.

Thus, the metallicity distributions of extragalactic GC systems and, more specifically, the existence or lack of a universal bimodality of [Fe/H] in ETGs, remains a matter of debate. Indirectly, when taken in the broader context of previous work, our analysis indicates that optical GC color bimodalities have different causes in different galaxies, with nonlinear color-metallicity relations playing an important role for some previously studied giant ellipticals. Finally, our study shows the effectiveness of optical-to-NIR colors as an unambiguous test for underlying metallicity bimodality.

Acknowledgements. Part of this work was supported by the FIRB-MIUR 2008 (P.I. G. Imbriani).

References

Ashman, K. M. & Zepf, S. E. 1992, ApJ, 384, 50
Bertin, E. & Arnouts, S. 1996, A&AS, 117, 393
Blakeslee, J. P., Cho, H., Peng, E. W., et al. 2012, ApJ, 746, 88
Brodie, J. P. & Strader, J. 2006, ARA&A, 44, 193
Brodie, J. P., Usher, C., Conroy, C., et al. 2012, ApJ, 759, L33
Cantiello, M. & Blakeslee, J. P. 2007, ApJ, 669, 982
Chies-Santos, A. L., Larsen, S. S., Cantiello, M., et al. 2012, A&A, 539, A54
Cohen, J. G., Blakeslee, J. P., & Ryzhov, A. 1998, ApJ, 496, 808
Côté, P., Marzke, R. O., & West, M. J. 1998, ApJ, 501, 554
Forbes, D. A., Brodie, J. P., & Grillmair, C. J. 1997, AJ, 113, 1652
Forte, J. C., Faifer, F., & Geisler, D. 2005, MNRAS, 357, 56
Jennings et al. 2013, in preparation, 1
Jordán, A., Blakeslee, J. P., Peng, E. W., et al. 2004, ApJS, 154, 509
Kissler-Patig, M. 1997, A&A, 319, 83
Kundu, A. & Zepf, S. E. 2007, ApJ, 660, L109
Kuntschner, H., Ziegler, B. L., Sharples, R. M., Worthey, G., & Fricke, K. J. 2002, A&A, 395, 761
Kurucz, R. L. 1993, in CD-ROM n. 15
Larsen, S. S. & Brodie, J. P. 2003, ApJ, 593, 340
Muratov, A. L. & Gnedin, O. Y. 2010, ApJ, 718, 1266
Peng, E. W., Jordán, A., Côté, P., et al. 2006, ApJ, 639, 95
Pietrinferni, A., Cassisi, S., Salaris, M., & Castelli, F. 2006, ApJ, 642, 797
Puzia, T. H., Kissler-Patig, M., Thomas, D., et al. 2005, A&A, 439, 997
Raimondo, G. 2009, ApJ, 700, 1247
Richtler, T. 2006, Bulletin of the A. S. of India, 34, 83
Schlafly, E. F. & Finkbeiner, D. P. 2011, ApJ, 737, 103
Schlegel, D. J., Finkbeiner, D. P., & Davis, M. 1998, ApJ, 500, 525
Schweizer, F. 1987, in Nearly Normal Galaxies. From the Planck Time to the Present, ed. S. M. Faber, 18–25
Tantalo, R., Chiosi, C., & Bressan, A. 1998, A&A, 333, 419
Tonry, J. L., Ajhar, E. A., & Luppino, G. A. 1990, AJ, 100, 1416
Tonry, J. L., Dressler, A., Blakeslee, J. P., et al. 2001, ApJ, 546, 681
Usher, C., Forbes, D. A., Brodie, J. P., et al. 2012, MNRAS, 426, 1475
VandenBerg, D. A., Brogaard, K., Leaman, R., & Casagrande, L. 2013, ApJ, 775, 134
Woodley, K. A., Harris, W. E., Puzia, T. H., et al. 2010, ApJ, 708, 1335
Worthey, G. 1994, ApJS, 95, 107
Yoon, S.-J., Sohn, S. T., Kim, H.-S., et al. 2013, ApJ, 768, 137
Yoon, S.-J., Sohn, S. T., Lee, S.-Y., et al. 2011, ApJ, 743, 149
Yoon, S.-J., Yi, S. K., & Lee, Y.-W. 2006, Science, 311, 1129

Table 2. Matched HAWK–I $JHKs$ photometry for all detected sources

ID	R.A. (J2000)	Dec. (J2000)	m_J (mag)	m_H (mag)	m_{Ks} (mag)	$\langle CS \rangle$
(1)	(2)	(3)	(4)	(5)	(6)	(7)
1	151.261846	-7.778326	14.532 ± 0.001	14.560 ± 0.001	14.832 ± 0.001	0.997
2	151.339249	-7.779547	15.262 ± 0.002	15.290 ± 0.001	15.713 ± 0.001	0.990
3	151.328988	-7.781540	13.407 ± 0.001	13.335 ± 0.001	13.949 ± 0.001	1.000
4	151.246152	-7.782556	20.196 ± 0.013	20.526 ± 0.018	21.869 ± 0.061	0.020
5	151.280919	-7.782237	19.050 ± 0.007	19.092 ± 0.006	19.317 ± 0.008	0.983
…	…	…	…	…	…	…

Notes. Columns list: (1) ID number; (2) right ascension; (3) declination; (4) $J-$band magnitude; (5) $H-$band magnitude; (6) K_s-band magnitude; (7) SExtractor mean $JHKs$ CLASS_STAR parameter.

Table 3. Results of GMM runs on GCs selected using criterion #1 (based on ΔCaT, see text).

color	p_1	p_2	σ_1	σ_2	N_{GC}	frac$_2$	$p(\chi^2)$	$p(DD)$	$p(kurt)$	DD	kurtosis
(1)	(2)	(3)	(4)	(5)	(6)	(7)	(8)	(9)	(10)	(11)	(12)
HS (HAWK-I+SLUGGS) sample											
$g-i$	0.794 ± 0.010	1.103 ± 0.013	0.055 ± 0.008	0.075 ± 0.010	73	0.531 ± 0.067	0.001	0.023	0.001	4.71 ± 0.48	-1.403
$g-J$	1.051 ± 0.038	1.672 ± 0.053	0.104 ± 0.020	0.231 ± 0.032	73	0.561 ± 0.076	0.001	0.118	0.001	3.47 ± 0.51	-1.241
$g-H$	1.034 ± 0.028	1.806 ± 0.040	0.143 ± 0.020	0.202 ± 0.031	73	0.524 ± 0.070	0.001	0.033	0.001	4.41 ± 0.52	-1.428
$g-Ks$	0.874 ± 0.064	1.736 ± 0.069	0.225 ± 0.051	0.232 ± 0.059	73	0.505 ± 0.095	0.001	0.078	0.001	3.77 ± 0.49	-1.273
$i-J$	0.263 ± 0.030	0.567 ± 0.057	0.065 ± 0.020	0.163 ± 0.027	73	0.587 ± 0.125	0.001	0.453	0.012	2.44 ± 0.58	-0.944
$i-H$	0.219 ± 0.023	0.679 ± 0.037	0.078 ± 0.016	0.156 ± 0.025	73	0.568 ± 0.080	0.001	0.080	0.001	3.74 ± 0.55	-1.364
$i-Ks$	0.096 ± 0.077	0.647 ± 0.068	0.195 ± 0.051	0.161 ± 0.051	73	0.465 ± 0.137	0.025	0.219	0.009	3.08 ± 0.49	-1.021
$J-Ks$	-0.164 ± 0.122	0.041 ± 0.056	0.157 ± 0.039	0.075 ± 0.031	73	0.364 ± 0.239	0.107	0.720	0.918	1.67 ± 0.88	0.536
$H-Ks$	-0.318 ± 0.118	-0.112 ± 0.032	0.114 ± 0.035	0.088 ± 0.022	73	0.919 ± 0.240	0.228	0.623	0.976	2.03 ± 1.44	1.018
$J-H$	-0.099 ± 0.054	0.057 ± 0.090	0.046 ± 0.023	0.086 ± 0.030	73	0.889 ± 0.303	0.862	0.535	0.708	2.26 ± 1.05	0.012
CaT	5.323 ± 0.254	7.705 ± 0.242	0.681 ± 0.230	0.745 ± 0.145	73	0.567 ± 0.110	0.010	0.156	0.005	3.34 ± 0.59	-1.062
HA (HAWK-I+ACS) sample											
$g_{F475W}-z_{F850LP}$	0.947 ± 0.014	1.361 ± 0.016	0.070 ± 0.011	0.126 ± 0.012	128	0.664 ± 0.048	0.001	0.065	0.001	4.06 ± 0.35	-1.254
$g_{F475W}-J$	1.072 ± 0.025	1.676 ± 0.032	0.099 ± 0.016	0.229 ± 0.022	128	0.681 ± 0.052	0.001	0.124	0.001	3.42 ± 0.35	-1.145
$g_{F475W}-H$	1.067 ± 0.035	1.779 ± 0.034	0.145 ± 0.027	0.224 ± 0.022	128	0.654 ± 0.051	0.001	0.086	0.001	3.78 ± 0.31	-1.147
$g_{F475W}-Ks$	0.869 ± 0.032	1.681 ± 0.035	0.153 ± 0.021	0.261 ± 0.028	128	0.679 ± 0.046	0.001	0.081	0.001	3.79 ± 0.35	-1.063
$z_{F850LP}-J$	0.127 ± 0.057	0.329 ± 0.085	0.070 ± 0.027	0.120 ± 0.037	128	0.666 ± 0.268	0.099	0.546	0.012	2.06 ± 0.50	-0.805
$z_{F850LP}-H$	0.119 ± 0.059	0.419 ± 0.024	0.089 ± 0.036	0.110 ± 0.026	128	0.640 ± 0.160	0.003	0.231	0.003	3.01 ± 0.72	-0.947
$z_{F850LP}-Ks$	-0.110 ± 0.061	0.299 ± 0.032	0.103 ± 0.037	0.163 ± 0.026	128	0.755 ± 0.114	0.011	0.201	0.038	3.00 ± 0.51	-0.655
$J-Ks$	-0.031 ± 0.094	-0.070 ± 0.183	0.047 ± 0.046	0.155 ± 0.052	128	0.820 ± 0.334	0.420	0.898	0.920	0.33 ± 1.81	0.475
$H-Ks$	-0.119 ± 0.048	-0.073 ± 0.039	0.098 ± 0.024	0.028 ± 0.024	128	0.151 ± 0.261	0.435	0.863	0.569	0.64 ± 0.94	-0.097
$J-H$	0.041 ± 0.048	0.324 ± 0.130	0.079 ± 0.024	0.034 ± 0.043	128	0.029 ± 0.377	0.013	0.029	0.987	4.65 ± 1.92	1.102
HSA (HAWK-I+SLUGGS+ACS) sample											
$g_{F475W}-z_{F850LP}$	0.938 ± 0.016	1.372 ± 0.020	0.068 ± 0.012	0.119 ± 0.022	58	0.555 ± 0.075	0.001	0.036	0.001	4.46 ± 0.63	-1.418
$i-z_{F850LP}$	0.139 ± 0.013	0.276 ± 0.013	0.040 ± 0.008	0.049 ± 0.009	58	0.596 ± 0.099	0.118	0.241	0.020	3.09 ± 0.44	-0.949
$g-i$	0.801 ± 0.030	1.114 ± 0.012	0.054 ± 0.031	0.074 ± 0.016	58	0.545 ± 0.085	0.001	0.013	0.001	4.86 ± 1.07	-1.446
$g_{F475W}-J$	1.065 ± 0.029	1.687 ± 0.060	0.112 ± 0.022	0.254 ± 0.040	58	0.558 ± 0.088	0.001	0.215	0.002	3.17 ± 0.60	-1.139
$g_{F475W}-H$	1.045 ± 0.037	1.794 ± 0.052	0.145 ± 0.026	0.239 ± 0.048	58	0.552 ± 0.080	0.001	0.097	0.001	3.79 ± 0.62	-1.266
$g_{F475W}-Ks$	0.892 ± 0.059	1.741 ± 0.074	0.236 ± 0.047	0.268 ± 0.064	58	0.506 ± 0.098	0.014	0.176	0.008	3.36 ± 0.54	-1.086
$z_{F850LP}-J$	0.127 ± 0.035	0.290 ± 0.087	0.038 ± 0.027	0.154 ± 0.043	58	0.657 ± 0.197	0.007	0.799	0.173	1.45 ± 1.08	-0.658
$z_{F850LP}-H$	0.133 ± 0.049	0.457 ± 0.056	0.103 ± 0.030	0.106 ± 0.030	58	0.454 ± 0.154	0.055	0.267	0.010	3.10 ± 0.66	-1.048
$z_{F850LP}-Ks$	0.042 ± 0.143	0.431 ± 0.133	0.227 ± 0.068	0.150 ± 0.059	58	0.260 ± 0.280	0.860	0.669	0.252	2.03 ± 0.62	-0.577
$g-J$	1.069 ± 0.025	1.714 ± 0.044	0.107 ± 0.017	0.223 ± 0.035	58	0.554 ± 0.078	0.001	0.111	0.001	3.68 ± 0.61	-1.315
$g-H$	1.045 ± 0.029	1.814 ± 0.040	0.134 ± 0.020	0.214 ± 0.034	58	0.556 ± 0.072	0.001	0.049	0.001	4.30 ± 0.63	-1.416
$g-Ks$	0.903 ± 0.068	1.769 ± 0.067	0.243 ± 0.050	0.230 ± 0.063	58	0.498 ± 0.096	0.004	0.116	0.001	3.66 ± 0.56	-1.230
$i-J$	0.302 ± 0.027	0.661 ± 0.062	0.087 ± 0.023	0.124 ± 0.033	58	0.424 ± 0.142	0.001	0.168	0.009	3.35 ± 0.80	-1.064
$i-H$	0.235 ± 0.026	0.686 ± 0.040	0.081 ± 0.018	0.159 ± 0.027	58	0.589 ± 0.077	0.001	0.127	0.001	3.57 ± 0.62	-1.335
$i-Ks$	0.111 ± 0.084	0.659 ± 0.089	0.203 ± 0.060	0.170 ± 0.056	58	0.460 ± 0.159	0.122	0.295	0.017	2.94 ± 0.56	-0.983
$J-Ks$	-0.169 ± 0.146	0.030 ± 0.052	0.159 ± 0.049	0.076 ± 0.030	58	0.394 ± 0.249	0.166	0.778	0.963	1.60 ± 1.23	0.874
$H-Ks$	-0.500 ± 0.118	-0.131 ± 0.055	0.023 ± 0.033	0.090 ± 0.025	58	0.983 ± 0.321	0.088	0.004	0.989	5.62 ± 1.57	1.380
$J-H$	-0.002 ± 0.079	0.098 ± 0.036	0.083 ± 0.029	0.054 ± 0.020	58	0.480 ± 0.297	0.475	0.800	0.584	1.44 ± 1.15	-0.194
CaT	5.693 ± 0.333	7.833 ± 0.290	0.836 ± 0.279	0.618 ± 0.149	58	0.504 ± 0.159	0.044	0.303	0.044	2.91 ± 0.67	-0.856

Notes. Columns list: (1) color; (2-3) mean and uncertainty of the first and second peaks in the double-Gaussian model; (4-5) width and uncertainty of the first and second peaks; (6) number of GC candidates selected; (7) fraction of GC candidates associated with the second, red, peak; (8-10) GMM p-values based on the likelihood-ratio test $p(\chi^2)$, peak separation $p(DD)$, and kurtosis $p(kurt)$, indicating the significance of the preference for a double-Gaussian over a single-Gaussian model (lower p-values are more significant); (11) separation of the peaks in units of the two Gaussian widths; (12) kurtosis of the distribution (DD≥2 and negative kurtosis are required for significative split between the two Gaussian distributions).

Table 4. Results of GMM runs on GCs selected using criterion #2 (based on Δ *color* and magnitude, see text).

color	p_1	p_2	σ_1	σ_2	N_{GC}	frac$_2$	$p(\chi^2)$	$p(DD)$	$p(kurt)$	DD	kurtosis
(1)	(2)	(3)	(4)	(5)	(6)	(7)	(8)	(9)	(10)	(11)	(12)
HS (HAWK-I+SLUGGS) sample											
$g-i$	0.783 ± 0.011	1.106 ± 0.013	0.060 ± 0.007	0.076 ± 0.011	68	0.521 ± 0.064	0.001	0.023	0.001	4.74 ± 0.54	-1.467
$g-J$	1.032 ± 0.083	1.672 ± 0.110	0.112 ± 0.057	0.251 ± 0.066	68	0.566 ± 0.144	0.001	0.167	0.001	3.30 ± 0.59	-1.292
$g-H$	1.014 ± 0.050	1.804 ± 0.067	0.167 ± 0.033	0.221 ± 0.051	68	0.500 ± 0.085	0.001	0.062	0.001	4.04 ± 0.57	-1.389
$g-Ks$	0.867 ± 0.083	1.710 ± 0.084	0.221 ± 0.058	0.261 ± 0.068	65	0.536 ± 0.112	0.003	0.134	0.003	3.49 ± 0.54	-1.210
$i-J$	0.308 ± 0.040	0.671 ± 0.072	0.101 ± 0.025	0.120 ± 0.034	69	0.375 ± 0.146	0.002	0.190	0.008	3.28 ± 0.66	-0.994
$i-H$	0.219 ± 0.034	0.697 ± 0.047	0.103 ± 0.022	0.155 ± 0.029	69	0.510 ± 0.084	0.001	0.114	0.001	3.63 ± 0.49	-1.309
$i-Ks$	0.068 ± 0.088	0.608 ± 0.085	0.189 ± 0.051	0.191 ± 0.055	69	0.502 ± 0.155	0.114	0.322	0.008	2.84 ± 0.43	-0.997
$J-Ks$	-0.234 ± 0.141	-0.028 ± 0.051	0.173 ± 0.059	0.104 ± 0.029	60	0.686 ± 0.240	0.100	0.798	0.977	1.45 ± 1.26	1.063
$H-Ks$	-0.147 ± 0.107	-0.074 ± 0.025	0.124 ± 0.046	0.031 ± 0.023	61	0.368 ± 0.210	0.013	0.845	0.988	0.82 ± 1.57	1.381
$J-H$	-0.128 ± 0.054	0.037 ± 0.095	0.027 ± 0.023	0.092 ± 0.028	67	0.919 ± 0.294	0.781	0.474	0.729	2.43 ± 1.01	0.019
CaT	5.246 ± 0.256	7.707 ± 0.257	0.828 ± 0.243	0.714 ± 0.129	69	0.523 ± 0.106	0.022	0.217	0.015	3.18 ± 0.51	-0.926
HA (HAWK-I+ACS) sample											
$g_{F475W}-z_{F850LP}$	0.931 ± 0.009	1.325 ± 0.018	0.060 ± 0.006	0.149 ± 0.010	252	0.596 ± 0.037	0.001	0.118	0.001	3.47 ± 0.29	-1.307
$g_{F475W}-J$	1.089 ± 0.048	1.699 ± 0.061	0.173 ± 0.056	0.214 ± 0.036	207	0.500 ± 0.097	0.001	0.127	0.002	3.14 ± 0.38	-0.711
$g_{F475W}-H$	1.034 ± 0.028	1.760 ± 0.032	0.170 ± 0.020	0.231 ± 0.021	215	0.563 ± 0.045	0.001	0.102	0.001	3.58 ± 0.24	-1.188
$g_{F475W}-Ks$	0.837 ± 0.025	1.670 ± 0.039	0.168 ± 0.028	0.300 ± 0.045	165	0.674 ± 0.050	0.001	0.118	0.038	3.43 ± 0.43	-0.573
$z_{F850LP}-J$	0.148 ± 0.033	0.364 ± 0.083	0.089 ± 0.028	0.122 ± 0.036	207	0.432 ± 0.238	0.003	0.424	0.183	2.03 ± 0.71	-0.348
$z_{F850LP}-H$	0.121 ± 0.037	0.442 ± 0.042	0.133 ± 0.028	0.122 ± 0.029	215	0.465 ± 0.136	0.021	0.282	0.022	2.51 ± 0.39	-0.586
$z_{F850LP}-Ks$	-0.080 ± 0.059	0.330 ± 0.028	0.150 ± 0.035	0.155 ± 0.025	168	0.645 ± 0.115	0.011	0.254	0.044	2.69 ± 0.48	-0.562
$J-Ks$	-0.086 ± 0.090	-0.018 ± 0.179	0.160 ± 0.044	0.055 ± 0.053	142	0.220 ± 0.312	0.255	0.845	0.909	0.57 ± 1.78	0.408
$H-Ks$	-0.128 ± 0.030	-0.072 ± 0.060	0.118 ± 0.029	0.031 ± 0.042	148	0.218 ± 0.203	0.046	0.845	0.983	0.65 ± 0.86	1.045
$J-H$	0.055 ± 0.092	0.030 ± 0.088	0.061 ± 0.031	0.110 ± 0.032	169	0.641 ± 0.319	0.577	0.908	0.904	0.28 ± 1.58	0.412
HSA (HAWK-I+SLUGGS+ACS) sample											
$g_{F475W}-z_{F850LP}$	0.917 ± 0.016	1.367 ± 0.025	0.065 ± 0.011	0.120 ± 0.022	56	0.573 ± 0.073	0.001	0.021	0.001	4.65 ± 0.68	-1.453
$i-z_{F850LP}$	0.140 ± 0.017	0.274 ± 0.018	0.030 ± 0.010	0.054 ± 0.011	56	0.630 ± 0.127	0.032	0.277	0.005	3.06 ± 0.59	-1.129
$g_{F475W}-i$	0.789 ± 0.027	1.116 ± 0.014	0.057 ± 0.025	0.071 ± 0.014	56	0.554 ± 0.082	0.001	0.008	0.001	5.07 ± 0.91	-1.477
$g_{F475W}-J$	1.052 ± 0.037	1.705 ± 0.069	0.124 ± 0.023	0.248 ± 0.042	56	0.554 ± 0.093	0.001	0.202	0.002	3.32 ± 0.63	-1.226
$g_{F475W}-H$	1.019 ± 0.044	1.807 ± 0.058	0.168 ± 0.028	0.229 ± 0.049	56	0.535 ± 0.080	0.001	0.074	0.001	3.92 ± 0.62	-1.294
$g_{F475W}-Ks$	0.835 ± 0.099	1.708 ± 0.104	0.245 ± 0.059	0.285 ± 0.077	56	0.542 ± 0.124	0.027	0.208	0.005	3.28 ± 0.50	-1.132
$z_{F850LP}-J$	0.182 ± 0.026	0.491 ± 0.061	0.105 ± 0.022	0.048 ± 0.034	56	0.185 ± 0.127	0.011	0.098	0.106	3.78 ± 0.84	-0.756
$z_{F850LP}-H$	0.114 ± 0.053	0.461 ± 0.059	0.114 ± 0.031	0.104 ± 0.032	56	0.438 ± 0.160	0.049	0.244	0.008	3.19 ± 0.54	-1.096
$z_{F850LP}-Ks$	-0.241 ± 0.153	0.222 ± 0.134	0.135 ± 0.073	0.228 ± 0.066	56	0.810 ± 0.287	0.718	0.498	0.175	2.47 ± 0.62	-0.675
$g-J$	1.056 ± 0.045	1.717 ± 0.066	0.119 ± 0.025	0.233 ± 0.041	56	0.571 ± 0.090	0.001	0.135	0.001	3.57 ± 0.61	-1.365
$g-H$	1.028 ± 0.057	1.818 ± 0.062	0.170 ± 0.040	0.222 ± 0.051	56	0.548 ± 0.091	0.001	0.063	0.001	4.00 ± 0.61	-1.393
$g-Ks$	0.913 ± 0.109	1.759 ± 0.079	0.262 ± 0.066	0.243 ± 0.062	53	0.540 ± 0.112	0.019	0.187	0.006	3.35 ± 0.60	-1.136
$i-J$	0.314 ± 0.036	0.697 ± 0.069	0.098 ± 0.023	0.105 ± 0.039	56	0.392 ± 0.144	0.001	0.099	0.003	3.77 ± 0.84	-1.152
$i-H$	0.258 ± 0.053	0.728 ± 0.061	0.130 ± 0.035	0.142 ± 0.038	56	0.494 ± 0.116	0.009	0.168	0.001	3.45 ± 0.59	-1.283
$i-Ks$	0.186 ± 0.134	0.687 ± 0.108	0.248 ± 0.077	0.168 ± 0.067	53	0.401 ± 0.220	0.419	0.561	0.075	2.36 ± 0.56	-0.836
$J-Ks$	-0.242 ± 0.113	-0.013 ± 0.040	0.178 ± 0.055	0.094 ± 0.025	47	0.661 ± 0.212	0.049	0.783	0.981	1.61 ± 1.08	1.141
$H-Ks$	-0.155 ± 0.093	-0.075 ± 0.022	0.124 ± 0.032	0.031 ± 0.020	49	0.346 ± 0.199	0.044	0.889	0.982	0.89 ± 1.23	1.256
$J-H$	-0.001 ± 0.069	0.104 ± 0.038	0.084 ± 0.028	0.051 ± 0.019	54	0.313 ± 0.301	0.770	0.787	0.379	1.51 ± 0.99	-0.437
CaT	5.661 ± 0.429	7.904 ± 0.325	1.091 ± 0.347	0.635 ± 0.168	56	0.447 ± 0.148	0.071	0.502	0.157	2.51 ± 0.70	-0.692

Notes. Columns list: same as in Table 3

Table 5. Results of GMM runs for the three Gaussian model with GCs selected using criterion #1.

color	p_1 (N_{GC}, σ)	p_2(N_{GC}, σ)	p_3(N_{GC}, σ)	$p(\chi^2)$	$p(DD)$	$p(kurt)$	DD	kurtosis
(1)	(2)	(3)	(4)	(5)	(6)	(7)	(8)	(9)
HS (HAWK-I+SLUGGS) sample (N_{GC}^{tot} = 73)								
$g-J$	1.063(34.5, 0.114)	1.472(6.5, 0.049)	1.746(32.0, 0.197)	0.001	0.033	0.001	4.67	-1.241
$i-J$	0.251(25.9, 0.058)	0.428(25.5, 0.112)	0.685(21.5, 0.111)	0.003	0.718	0.012	1.99	-0.944
$i-H$	0.221(32.4, 0.078)	0.475(7.1, 0.033)	0.732(33.5, 0.120)	0.001	0.098	0.001	4.23	-1.364
CaT	5.064(13.1, 0.285)	6.162(29.8, 1.141)	7.881(30.1, 0.681)	0.019	0.89	0.005	1.32	-1.062
HA (HAWK-I+ACS) sample (N_{GC}^{tot} = 128)								
$g-z$	0.951(44.6, 0.073)	1.177(8.5, 0.027)	1.388(74.8, 0.107)	0.001	0.118	0.001	4.11	-1.254
$g-J$	1.078(43.1, 0.102)	1.412(8.1, 0.060)	1.718(76.8, 0.206)	0.001	0.136	0.001	4.00	-1.145
$g-Ks$	0.878(42.6, 0.159)	1.636(73.1, 0.215)	2.023(12.2, 0.185)	0.001	0.11	0.001	4.01	-1.063
$z-J$	0.123(45.7, 0.068)	0.313(72.5, 0.094)	0.521(9.8, 0.024)	0.036	0.444	0.012	2.32	-0.805
$z-H$	0.110(44.2, 0.081)	0.264(8.9, 0.025)	0.435(74.9, 0.099)	0.01	0.449	0.003	2.58	-0.947
HSA (HAWK-I+SLUGGS+ACS) sample (N_{GC}^{tot} = 58)								
$g_{F475W}-J$	1.069(26.6, 0.114)	1.629(25.6, 0.191)	2.035(5.8, 0.112)	0.007	0.173	0.002	3.56	-1.139
$g_{F475W}-H$	1.042(25.4, 0.144)	1.801(6.7, 0.071)	1.779(25.9, 0.278)	0.005	0.009	0.001	6.69	-1.266
$g_{F475W}-Ks$	0.956(33.2, 0.278)	2.107(6.6, 0.158)	1.705(18.1, 0.116)	0.066	0.042	0.008	5.09	-1.086
$z_{F850LP}-J$	0.126(32.9, 0.059)	0.290(13.7, 0.038)	0.479(11.3, 0.054)	0.007	0.177	0.173	3.33	-0.658
$z_{F850LP}-H$	-0.026(3.7, 0.035)	0.148(27.1, 0.084)	0.452(27.3, 0.108)	0.237	0.437	0.01	2.70	-1.048
$z_{F850LP}-Ks$	-0.162(17.2, 0.152)	0.058(9.9, 0.044)	0.340(30.9, 0.175)	0.745	0.754	0.252	1.97	-0.577
$g-J$	1.075(27.0, 0.111)	1.462(6.8, 0.042)	1.807(24.2, 0.167)	0.001	0.061	0.001	4.63	-1.315
$g-H$	1.046(26.1, 0.134)	1.497(5.4, 0.041)	1.884(26.6, 0.162)	0.001	0.081	0.001	4.55	-1.416
$i-J$	0.275(27.5, 0.069)	0.422(6.3, 0.030)	0.666(24.2, 0.119)	0.009	0.423	0.009	2.77	-1.064
$i-H$	0.241(25.1, 0.084)	0.488(6.0, 0.030)	0.745(26.9, 0.119)	0.001	0.105	0.001	3.92	-1.335

Notes. Columns list: (1) color; (2-4) first, second and third peaks in the three Gaussian model, numbers within parentheses are the number of GCs associated with each peak, and the width of the distribution; (5-7) GMM p-values, as in Table 3; (8) separation of the peaks in units of the three Gaussian widths; (9) kurtosis of the distribution